In-depth characterization of as-deposited and annealed Fe-Wcoatings electrodeposited from glycolate-citrate plating bath

A. Mulone [a], A. Nicolenco [b], V. Hoffmann [c], U. Klement [a, **], N. Tsyntsaru [b, d], H. Cesiulis [b, *]

[a] Chalmers University of Technology, Department of Industrial and Materials Science, Gothenburg, Sweden
[b] Vilnius University, Department of Physical Chemistry, Lithuania
[c] Leibniz Institute for Solid State and Materials Research Dresden, Dresden, Germany
[d] Institute of Applied Physics of ASM, Chisinau, Republic of Moldova

Keywords: Electrodeposition, Tungsten alloys, Iron alloys, GD-OES, Thermal stability

a b s t r a c t

Fe-W coatings with 4, 16 and 24 at.% of W were electrodeposited under galvanostatic conditions from a new environmental friendly Fe(III)-based glycolate-citrate bath. This work aims to find correlations between composition including the light elements, internal structure of the electrodeposited Fe-Walloys and functional properties of material. The obtained alloys were characterized by Glow Discharge Optical Emission Spectrometry (GD-OES), Scanning Electron Microscopy (SEM) with Energy Dispersive X-ray Spectroscopy (EDS), Transmission Electron Microscopy (TEM), and X-ray Diffraction (XRD). Compositional depth profiles of 10 mm thick coatings obtained by GD-OES show that the distribution of metals is uniform along the entire film thickness, while SEM imaging depicted the presence of cracks and O- and W-rich areas inside the Fe-Wcoating with 4 at.% W. In the samples with 16 and 24 at.% of W, oxygen and hydrogen are present mostly at the surface about 1 mm from the top while traces of carbon are distributed within the entire coatings. With increasing W content, the structure of the coatings changes from nanocrystalline to amorphous which was shown by XRD and TEM analysis. Also, the surface of coatings becomes smoother and brighter, that was explained based on the local adsorption of intermediates containing iron and tungsten species. Annealing experiments coupled with XRD analysis show that the thermal stability of Fe-W alloys increases when the W content increases, i.e. the coating with 24 at.% W retains the amorphous structure up to 600 _C, where a partially recrystallized structure was observed. Upon recrystallization of the amorphous samples the following crystalline phases are formed: a-Fe, Fe_2W, Fe_3W_3C, Fe_6W_6C, and $FeWO_4$. Hence, the Fe-W coatings with higher W content (>25 at.%) can be considered as suitable material for high temperature applications.

1. Introduction

The interest in W alloys has continuously grown due to their advantageous properties. The addition of tungsten to iron group metals improves the properties of alloys such as hardness, corrosion resistance and thermal stability [1e4]. For these reasons W alloys with Fe, Co and Ni can represent an alternative to hard chromium coatings which are deposited using carcinogenic compounds (i.e. Cr^{6+}) [5]. In the past, electrochemical studies were concentrated mostly on Ni-W and Co-W alloys, while the investigations on electrodeposited Fe-W coatings are rather scarce. As the use of Co and Ni is more and more discouraged because of environmental issues, the electrodeposition of Fe-based alloys has gained in importance.
However, electrodeposition of Fe-W alloys is usually associated

with low current efficiency. It could be attributed to the fast oxidation of Fe^{2+} to Fe^{3+} (when Fe(II)-based electrolyte is used) and higher cathodic polarization of Fe-W alloys (above _1.00 V) as compared to Ni-W or Co-W (_0.65 ÷ _1.00 V), which results in a higher partial current density of side reaction [2,6]. Moreover, as was shown in Ref. [7], the electrolytes based on Fe(II) compounds are unstable thermodynamically and are governed by the Fe(II) oxidation kinetics. Most recent successful attempts to obtain Fe alloys with refractory metals from Fe(III) electrolytes were reported [8e10]. Nonetheless, the current efficiency of the deposition in referred studies did not exceed 40% [9,11].

The appropriate electrodeposition conditions influence the composition and structure of electrodeposited alloys. Thus, the W content in electrodeposited alloys can vary within a wide range, depending on the deposition conditions, but usually it does not exceed 30e35 at.% [12]. Generally, the structure of W-containing alloys with iron group metals tends to transit from nanocrystalline to “amorphous-like” with increase in W content in the alloy [12]. Thus, Fe-W alloys can be deposited with an amorphous [13] or nanocrystalline structure [14]. This tunable structure represents a useful opportunity when aiming for certain properties of interest. As a matter of fact the nanocrystalline W alloys are characterized with higher saturation magnetization [15] while amorphous alloys usually exhibit higher hardness and corrosion resistance [16].

As a novel approach, an environmental friendly and thermodynamically stable glycolate-citrate bath was employed for Fe-W alloys, which allowed to produce Fe-W coatings with up to 60e70% of current efficiency from Fe(III)-based solution [7,17]. An increase of current efficiency in this electrolyte was associated with specific complexes distribution of Fe and W, and we were able to produce Fe-rich and W-rich Fe-W alloys with tunable mechanical and magnetic properties by fine control of the deposition conditions.

However, it was observed that the tungsten content is not the sole factor influencing the structure and properties of the electrodeposited alloy. During the electrodeposition, various non-metallic elements can be incorporated and alter grain growth and influence the microstructure development during the thermal treatment [18,19].

Former works on W alloys with iron group metals show that after a thermal treatment the microhardness and corrosion resistance of electrodeposits increases due to formation of stable intermetallic compounds (Fe_2W), which is usually observed at temperatures higher than 400 _C [6,20,21].

The effects of heat treatments on compositional and structural

features of the deposited W alloys considering various tungsten contents and the co-deposited impurities have been studied most extensively for Ni-W alloys [18,19,22e27]. While scarce literature on Fe-W alloys electrodeposited from citrate-ammonia baths shows better thermal stability properties as compared to other W alloys with Ni and Co, retaining the nanocrystalline structure after annealing up to 700e800 _C [14].

The quantification of incorporated co-deposited non-metallic elements seems to be a crucial step towards characterization of functional materials. Typically, electrodeposition of metal alloys from aqueous solutions occurs along with abundant hydrogen evolution on the cathode. This leads to a local increase in pH at the electrode/solution interface and may cause the formation of insoluble hydroxides which become incorporated in the coating [28].

The precipitation of hydroxides at the electrode/solution interface with the layer growth is expected to have an impact on the physical and chemical properties of the obtained deposits [29].

Also, carbon is a common impurity in electrodeposited coatings. Its incorporation is often related to the organic additives used in the electrolytic bath [30]. Carbon presence within the alloy can lead to carbide phase precipitation during annealing with important implications both for the thermal stability and the mechanical properties of the coating [19]. The presence of oxygen as impurity and its effect on both thermal stability and mechanical properties has also been investigated for Ni-W alloy [18].

However, the quantitative determination of the full composition of electrodeposits often is a challenge. It is a well-known that EDS analysis has limitations with respect to quantification of light elements and low concentrations due to two main points: (i) elements with $Z < 11$ emit low energy X-rays which are subject to strong absorption by the specimen; and (ii) the yield of fluorescence increases with the atomic number and de-excitation of light elements occurs mainly by the emission of Auger electrons.

Therefore, meeting the existing demand for the quality control of functional materials, Glow Discharge Optical Emission Spectroscopy (GD-OES) can be applied for accurate composition analysis. Whereas the qualitative measurement of the light element depth distribution by GD-OES has been recognized as a powerful tool for reliable in-depth analysis, it is known that quantitative compositional depth profiling of light elements, especially of H and O, is very challenging [31]. No matrix-sensitive calibration material is available and matrix independent calibration make it uncertain. Therefore, in this study sintered calibration samples for O [32] and H [33] produced at IFW Dresden were used for multi-matrix calibration

for the first time.
The aim of this paper is to study the interdependences between the composition and structure of Fe-W coatings by use a new analytical strategy and techniques including Scanning Electron Microscopy (SEM) with Energy Dispersive X-ray Spectroscopy (EDS), Transmission Electron Microscopy (TEM), GD-OES, and X-ray Diffraction (XRD) analysis. Furthermore, the annealing effects on the structure and morphology of the produced Fe-W alloys with different amounts of W are also studied. To the best of our knowledge, in depth characterization of electrodeposited Fe-W alloys and incorporation of light elements into deposits have not been performed before.

2. Experimental

2.1. Electrodeposition of Fe-W alloys

In our previous work [17] the influence of tungstate concentration and deposition parameters (current density, pH, temperature) on induced codeposition of W with Fe from recently developed glycolate-citrate Fe(III)-based electrolyte was studied. Fe-W samples with various W content from few at.% to 25 at.% can be deposited in a controlled way by changing electrodeposition parameters. At 65 _C the partial current for W deposition is higher than that for room temperature, which results in the increase of W content in the deposit at these conditions. Based on the published data [17], Fe-W coatings with 4, 16 and 24 at.% of W have been obtained from the electrolyte with following composition: 1 M glycolic acid, 0.3 M citric acid, 0.1 M $Fe_2(SO_4)_3$ and 0.3 M Na_2WO_4. The deposition conditions are given in Table 1. The bath pH was adjusted by addition of either NaOH or H_2SO_4. The cathodic current density of 15 mA cm_{-2} was applied as is the optimum for Fe-W alloys deposition from electrolyte used [17]. Electrodeposition of thin films was performed in a typical three-electrode cell. A pure copper sheet was used as the working electrode. Platinized titanium was used as a counter electrode, and saturated $Ag/AgCl/KCl_{sat}$ was used as reference electrode and all potential values are presented in respect of this electrode. The deposition current efficiency was calculated based on the Faraday's law as described elsewhere [17].

Table 1
Operating conditions and EDS chemical composition of as-deposited Fe-W coatings

Sample	T, °C	pH	j, mA cm^{-2}	CE, %	-E, V	Composition (at.%)				
						Fe	W	O	Fe	W
1	20	6.5	15	24	1.25	80	4	16	96	4
2	65	5.0	15	50	1.04	59	10	31	84	16
3	65	6.5	15	72	1.08	64	20	17	76	24

2.2. Coating characterization

Secondary electron imaging was used to acquire the images of the as-plated surfaces by using a Leo 1550 Gemini SEM with field emission gun and the cross-sectional images were acquired using back-scattered electrons. The chemical composition was measured both at the surface and on cross-sections of the samples using EDS and an accelerating voltage of 20 kV, the obtained results are shown in Table 1. TEM investigation was performed with a Zeiss EM 912 OMEGA microscope operating at an accelerating voltage of 120 kV. The depth profiling analysis was carried out using a GDA750HR (Spectruma) with 2.5 mm source in DC mode. The discharge was operated in a high-purity Ar 5.0 atm and constant current (10 mA)/ constant voltage (700 V) control mode.
The calibration samples for GD-OES analysis were chosen in a way that a wide element concentration range was covered for further quantification. The sputtering rate factor of self-made calibration samples (ratio of the sputtering rate of the sample to the sputtering rate of Fe) was determined by density and crater volume measurements [34]. The wavelengths of the selected spectra emission lines were: 371 nm for Fe, 429 nm for W, 219 nm for Cu, 165 nm for C, 777 nm for O, and121 nm for H. With help of sintered calibration samples with Cu, Mg and Al matrix for O produced at IFW Dresden [32] the matrix dependence of the emission yield of the O I 130.22 nm line was revealed [35]. The different emission yield of this line is caused by a strong line shift effect reported by K€oster [36]. Therefore, Gonzalez-Gago et al. [35] proposed to use the oxygen triplet at 777 nm to overcome this problem.
We have now confirmed the matrix independence of the line O I 777,194 nm for O in Cu, Mg and Al and a CDP of a 3.5 mm thick iron oxide layer with mainly Fe_3O_4 (28 wt.% O) revealed 33 wt.% O and the correct thickness. Systematic errors for the O value smaller than 30% are estimated. The emission yield of H was obtained with help of sintered calibration material with TiH_2 and ZrH_2 in Cu matrix

[33]. It turned out [37] that these samples allow the reproducible quantification of less than 0.3 wt.% H in Cu matrix using the lines H I 121,567 nm, H I 486,135 nm and H I 656,279 nm.
Fig. 1 shows the calibration curves obtained for the elements Fe, W and O in constant voltage (700 V)/constant current (10 mA) mode. The calibration also included Na, S and N, although they were not observed in the EDS measurement. H, O and Na were calibrated with sintered calibration samples of IFW. Four Fe-W calibration samples were produced by melting and characterized by Inductively Coupled Plasma Optical Emission Spectroscopy (ICPOES). The crystallographic structure and phase composition of the obtained coatings were identified by means of a Rigaku MiniFlex II diffractometer with Cu Ka radiation (l ¼ 1.54183 Å) operated at 30 kV and 30 mA.
Vacuum annealing of the samples was performed in a controlled vacuum chamber (1 _ 10_8 Pa) keeping the samples at 200 _C, 400 _C, 600 _C and 800 _C for 1 h. Samples were afterwards cooled down to room temperature inside the furnace.

3. Results and discussion

3.1. Characterization of as-plated Fe-W coatings: surface morphology, composition and crystallographic structure

SEM micrographs of the as-plated coatings with increasing W content are shown in Fig. 2a-c together with the cross-section of each sample after metallographic preparation (Fig. 2d-f).
By increasing the W content in the coatings the surface morphology is strongly influenced. The surface of the low W-containing sample is characterized with a globular morphology resembling a cauliflower structure. The other two deposited samples show a smooth surface. Some superficial cracks observed for the W-rich samples can be inferred to the higher amount of W which leads to increased internal stresses in the coating and formation of microcracks [1,3].
Interestingly, the smoothening and leveling effect was achieved without using additives in the plating bath by fine control of the deposition parameters. Namely, it requires such values of overpotential that can ensure rather high crystallization and nucleation rate, but not too fast charge transfer [38]. In addition, the electrodeposition of W alloys with iron group metals occurs via formation of intermediate electroactive mixed complex which absorbed on the cathode surface at the first step and is subsequently reduced at the downstream steps [39,40]. Probably, adsorption of these complexes

is localized on the blisters. The surface coverage by intermediates shall be partial and strong enough without possibility to migrate to the sites. Adsorbed intermediates are formed from the relatively big species, which preferentially are: at pH 5 -$WO_2Gly_2^{2-}$, $FeH_2(Cit)_2^{3-}$, $FeH(Cit)_2^{4-}$; at pH 6.5 - $WO_2Gly_2^{2-}$ and $FeH(Cit)_2^{4-}$ [7]. These adsorbed intermediate complexes act as leveling or brightening agents. In general case [38], during the electrodeposition of tungsten or molybdenum alloys with iron group metals the leveling and refining is accompanied by refinement of the deposits in regard to crystallite size with increase in refractory metal content in the alloys [12,25].

In Table 1, the chemical composition of the different samples measured by EDS on the sample surfaces is reported. Electrodeposited tungsten alloys normally contain some oxygen that is incorporated in form of oxides mainly in the top surface layer [13] but also within the coating, forming tungsten oxide streaks [18,41]. As it is seen from Table 1, there is no direct correlation between the Wand O content in the alloy (as well as there is no clear influence of the deposition conditions). It is worth noticing that it is rather difficult to reproduce the data of the O content, while the tungsten content is constant when applying certain deposition conditions. Taking this into account, the composition of alloys is more correct to present as content of the metallic phase only (right column of Table 1). This assumption can be partially confirmed by the cross section analysis of the three samples shown in Fig. 2d-f. In the cross-section of the low W containing sample (Fig. 2d) internal vertical cracks and nests of smaller cracks are seen. These nests appear predominantly at a certain distance from the substrate surface, probably due to the local increase in pH at the electrode/ solution interface. The areas around these cracks appear brighter indicating a variation of chemical composition. The presence of these cracks seems also to influence the further growth of the film leading to a columnar-like growth. Fig. 3 shows the EDS line scan performed along one of the nests of cracks observed in Fig. 2d. The cracks appear to be in an O- and W-rich area and the brighter area around it is probably due to W segregation.

On the other hand, the cross-sections of the two samples with Higher W content appear to be crack-free. Both cross-sections show the presence of contrast variations aligned horizontally with respect to the substrate. The contrast can be interpreted as a small local variation of the chemical composition along the thickness of the samples. However, a chemical variation is not revealed by the EDS line scan performed along both samples. Instead, a homogenous elemental distribution is observed, i.e. without any W- or O enrichment as in the case of the Fe-W sample with 4 at.% W.

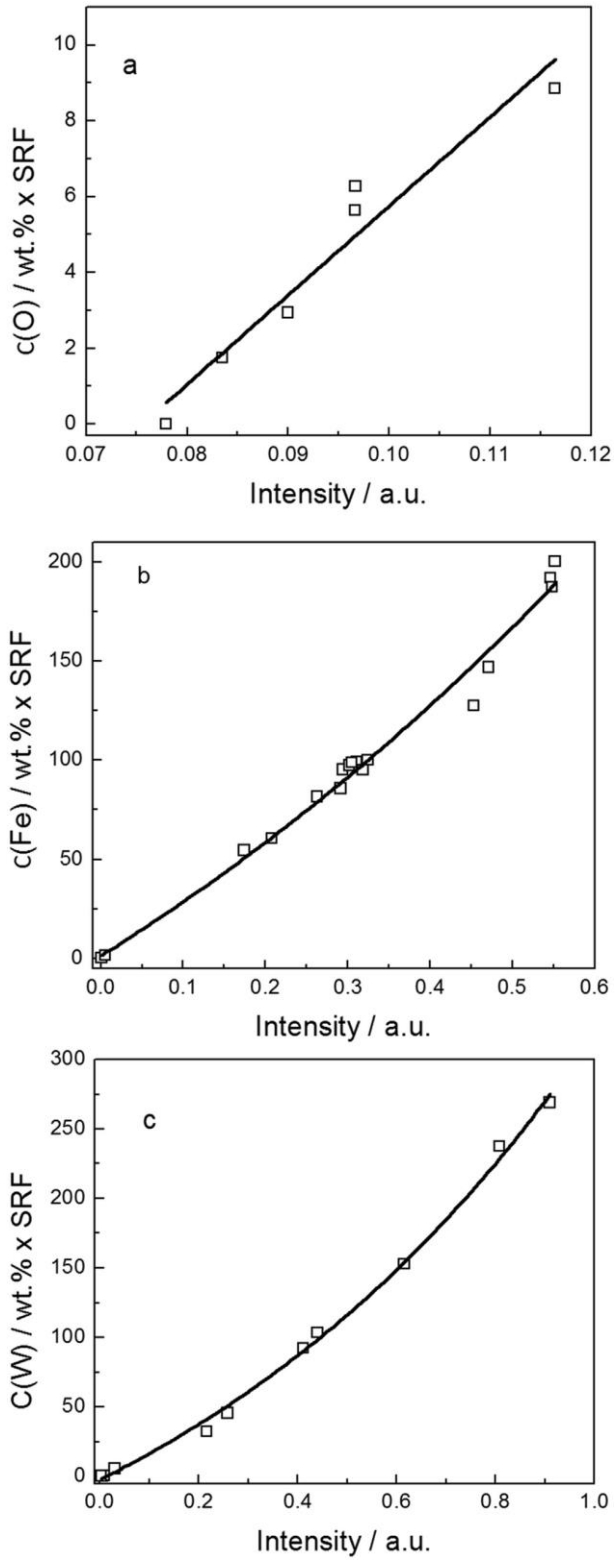

Fig. 1. GD-OES calibration curves for O 777 (a), Fe 371 (b) and W 429 (c). SRF- sputtering rate factor.

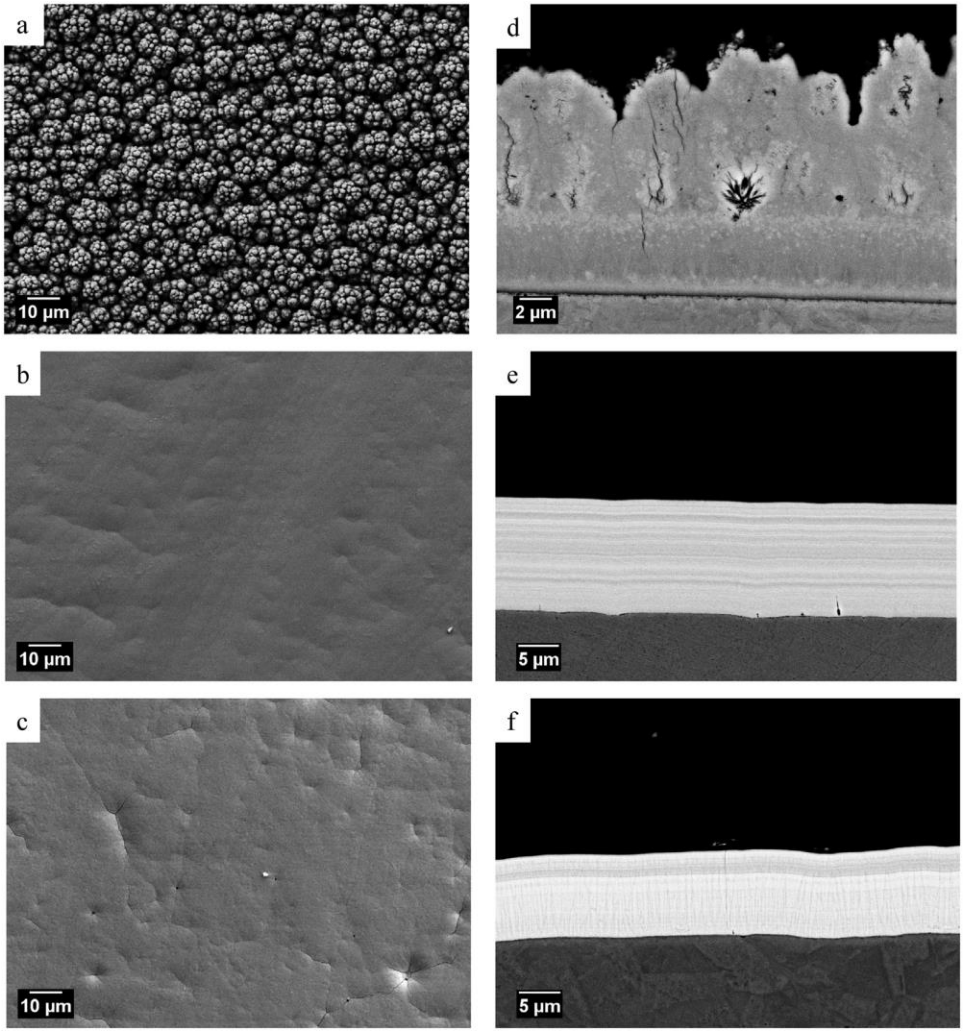

Fig. 2. Secondary electron images of the surface morphology of the 4 at.% W (a), 16 at.% W (b), and 24 at.% W samples (c); back-scattered electrons images of the cross-sections of the 4 at.% W (e), 16 at.% W (e), and 24 at.% W samples (f).

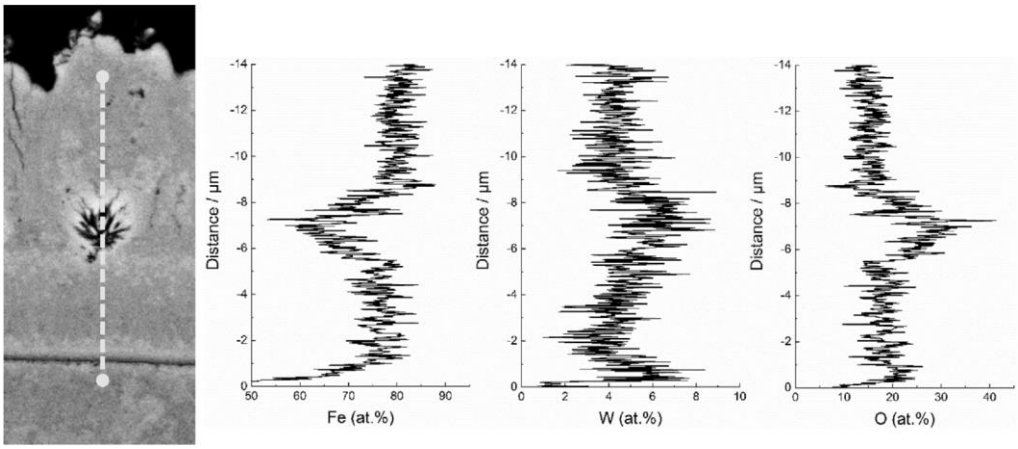

Fig. 3. EDS line scan along one of the nest of cracks observed on the cross-section of Fe-W coating with 4 at.% of W.

Furthermore, the oxygen quantity measured from the cross section of the sample with 16 at.% W is strongly reduced with respect of the amount registered from the surface analysis, and in the case of the 24 at.% W sample oxygen is not even detected. These findings support the assumption of oxygen only being present at the surface in the case of the higher W content sample. Thus, increasing the W content in the coatings seems to stabilize the deposition of the Fe-W alloys and decreases the crack formation and oxygen incorporation during the alloy deposition.
The O content determined by EDS analyses is rather qualitative than quantitative and the results provide the composition not deeper than approx. 1 mm from the analyzed surface. Yet, for understanding and thorough evaluation of functional properties of the Fe-W alloys, it is important to know their bulk composition. However, the quantitative determination of the full composition of electrodeposits including incorporated non-metallic elements such as O, H and C is a methodical challenge. Therefore, in this study, the experiments were carried out by means of GD-OES in order to get reliable compositional depth profiles (CDP) to determine if O is codeposited with Fe and W or it is mainly present on the surface.

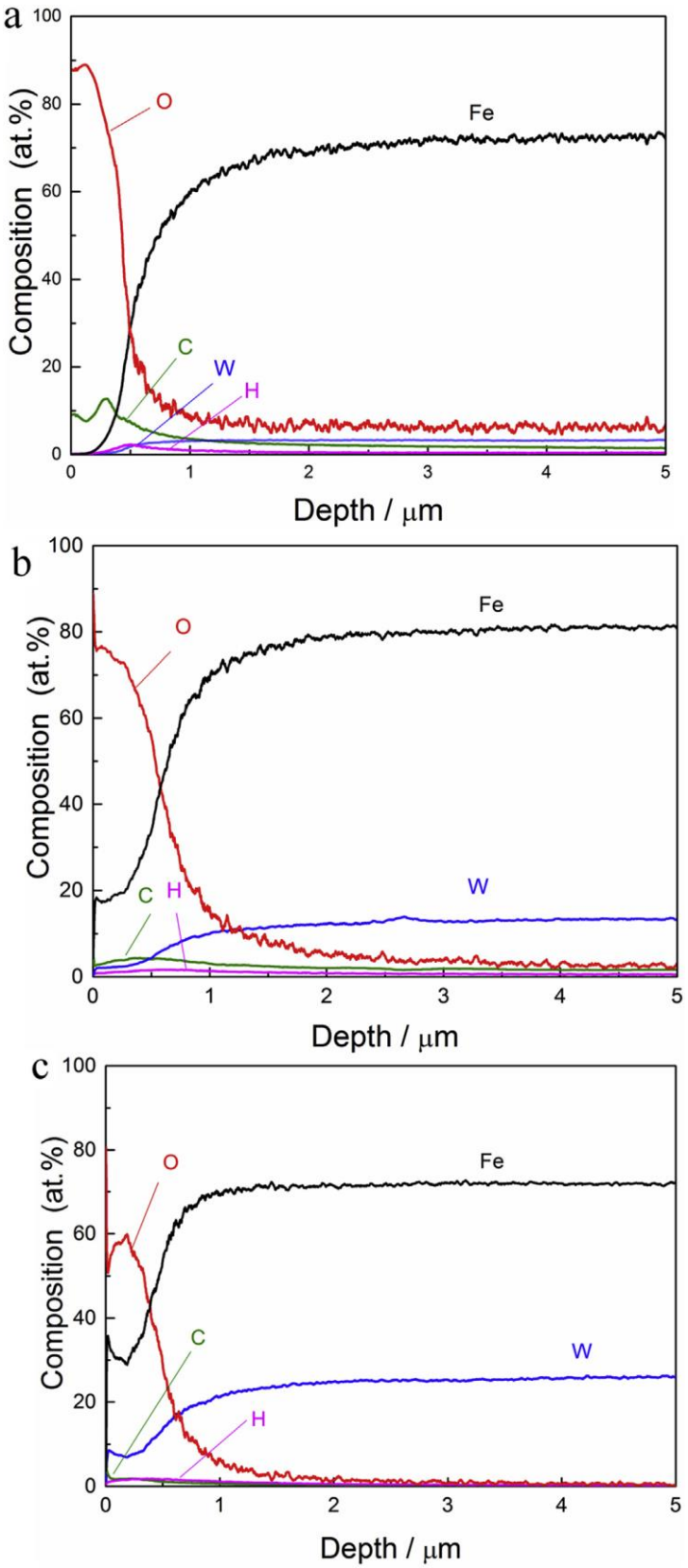

Fig. 4. Compositional depth profiles as obtained by GD-OES of Fe-W samples of different composition: 4 at.% of W (a), 16 at.% of W (b) and 25 at.% of W(c).

Representative examples of the CDPs obtained for the Fe-W samples under investigation are shown in Fig. 4. The Fe-W alloys of different composition are characterized by a strongly oxidized top surface layer of ~1-2 mm thickness. The surface layer consists mainly of O and Fe and contains relatively high amounts of C and H, as compared to the concentration deeper down in the material. Nevertheless, the distribution of both Fe and W inside the layers is constant, demonstrating a homogeneous growth of the alloy during electrodeposition independent of deposition temperature and plating pH. Small composition fluctuations are visible in the obtained GD-OES curves, which would resemble the composition variations aligned horizontally with respect to the substrate observed in the cross-section of the two samples with higher W content (Fig. 2 d-f). Studies on similar banded structures found on the cross-sections of electrodeposited Fe-alloys suggest that these structures are formed due to variation/incorporation of light impurities, i.e. oxygen and hydrogen, during the plating process [42]. However, it is hard to directly relate the fluctuations observed in the GD-OES curves to the banded structure observed by cross sections imaging. As a matter of fact, the length-scale of such banded features (few hundreds of nm) is in the range of the depth resolutions limits of the performed GD-OES measurements. Even if in small amounts, the GD-OES results show that C is present in the bulk of the three deposited coatings. For the samples with 4 at.% W and 16 at.% W, the C content is varying between 1.5 and 2.5 at.% up to 5 mm below the surface, while for the sample with 24 at.% W, at the same distance from the sample surface the carbon is ranging from 0.2 to 0.4 at.%. The carbon co-deposition can be attributed to the inclusion of a reaction intermediate derived from organic acids. In the case of the electrolytic bath used in this study, the presence of carbon is due to the incorporation of some organic species while depositing the Fe-W coating from a solution containing organic ligands [43]. The measured profiles were also investigated for Na

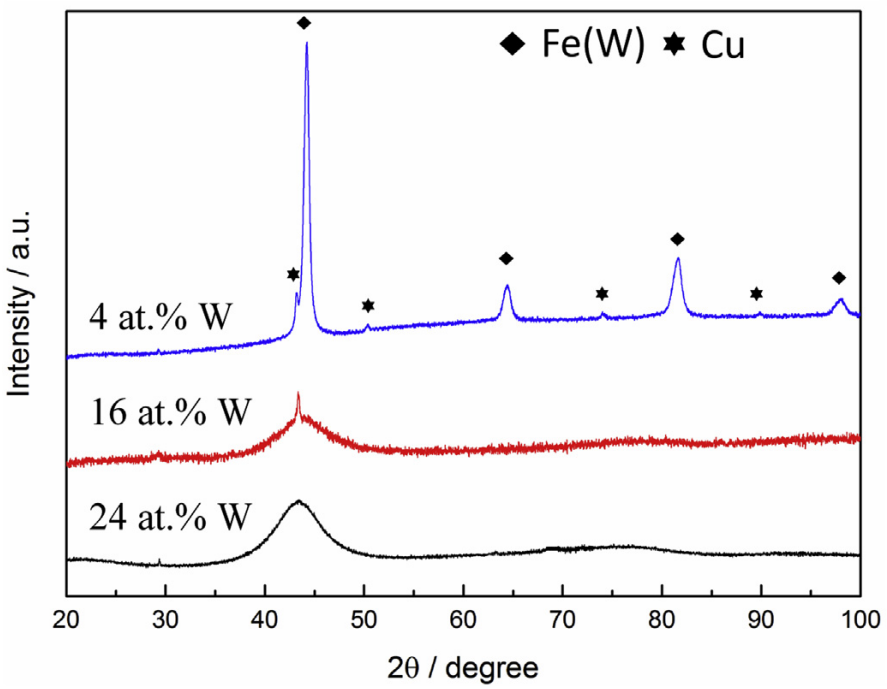

Fig. 5. X-ray diffraction profiles of the as-deposited Fe-W sample.

and S content. However, no noticeable influence from these elements was observed in the quantification of the investigated samples. They have been observed by GD-OES but at concentrations lower than 0.2 at.%, which has not much influence on the layer properties and therefore these elements are not discussed.

A drastic decrease in the concentration of oxygen within first few microns was observed. Therefore, the nature of the top surface layer seems to be the spontaneous chemical oxidation due to the contact of alloy's surface with corrosive medium (electrolyte, water, air). Also, it is supposed that some H and C atoms remain adsorbed on the electrode surface and thus can be rather considered as impurities. However, some recent investigations have shown that certain minor contamination elements can interact strongly with the alloy and alter grain growth and microstructure development during annealing [3,19].

In Fig. 4a, the quantitative depth profile of the Fe-W sample deposited at room temperature is shown. In this case, O is not only present on the surface, but also homogeneously distributed in the interior of the layer. With about 7 at.%, the oxygen content in the alloy deposited at room temperature is considerably higher as compared to the O content in the interior of alloys deposited at 65 _C (Fig. 4b and c). According to the model proposed by V.

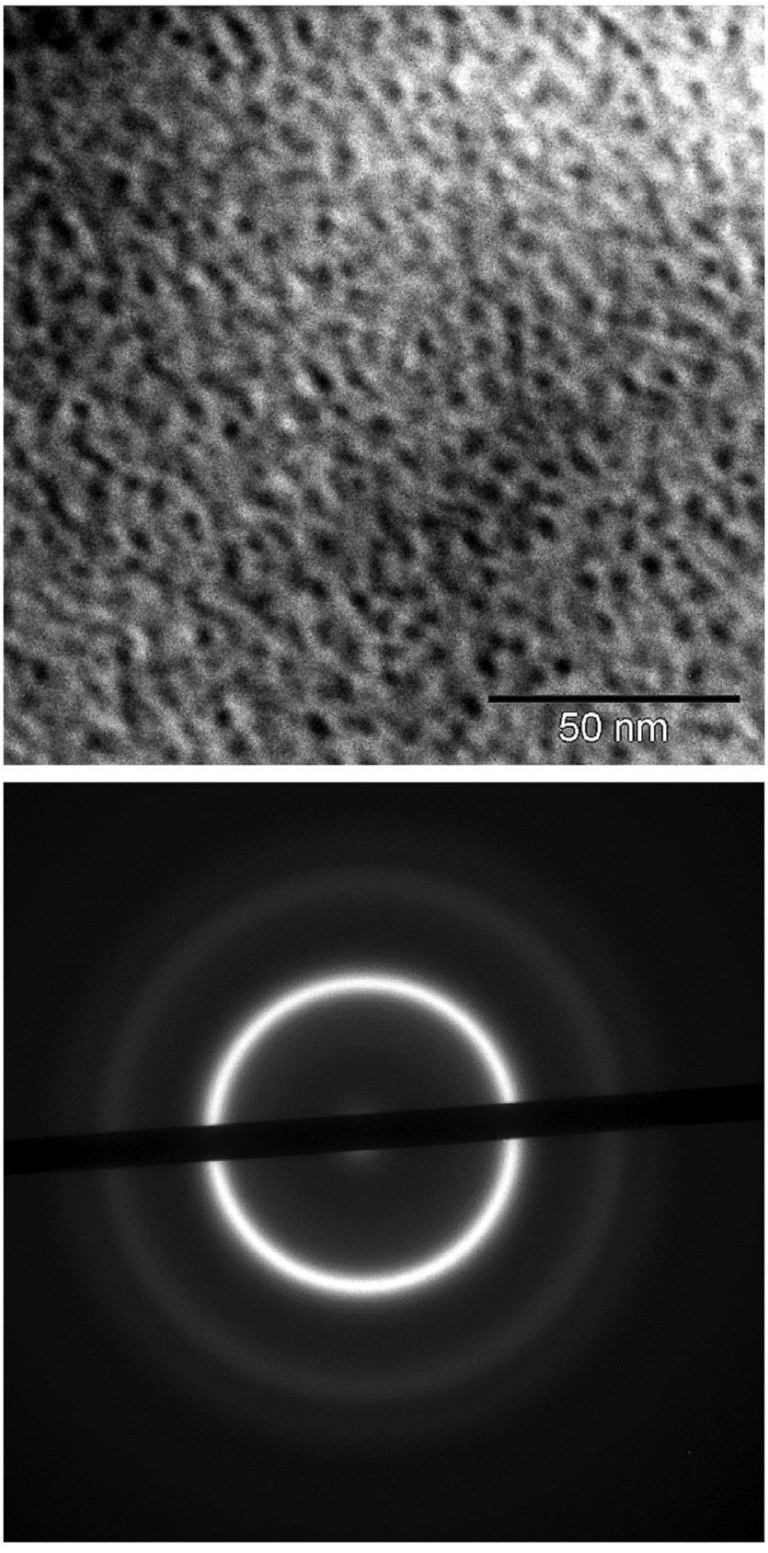

Fig. 6. TEM image of the electrodeposited sample with 24 at.% of W (a), and SAD pattern of the same sample (b).

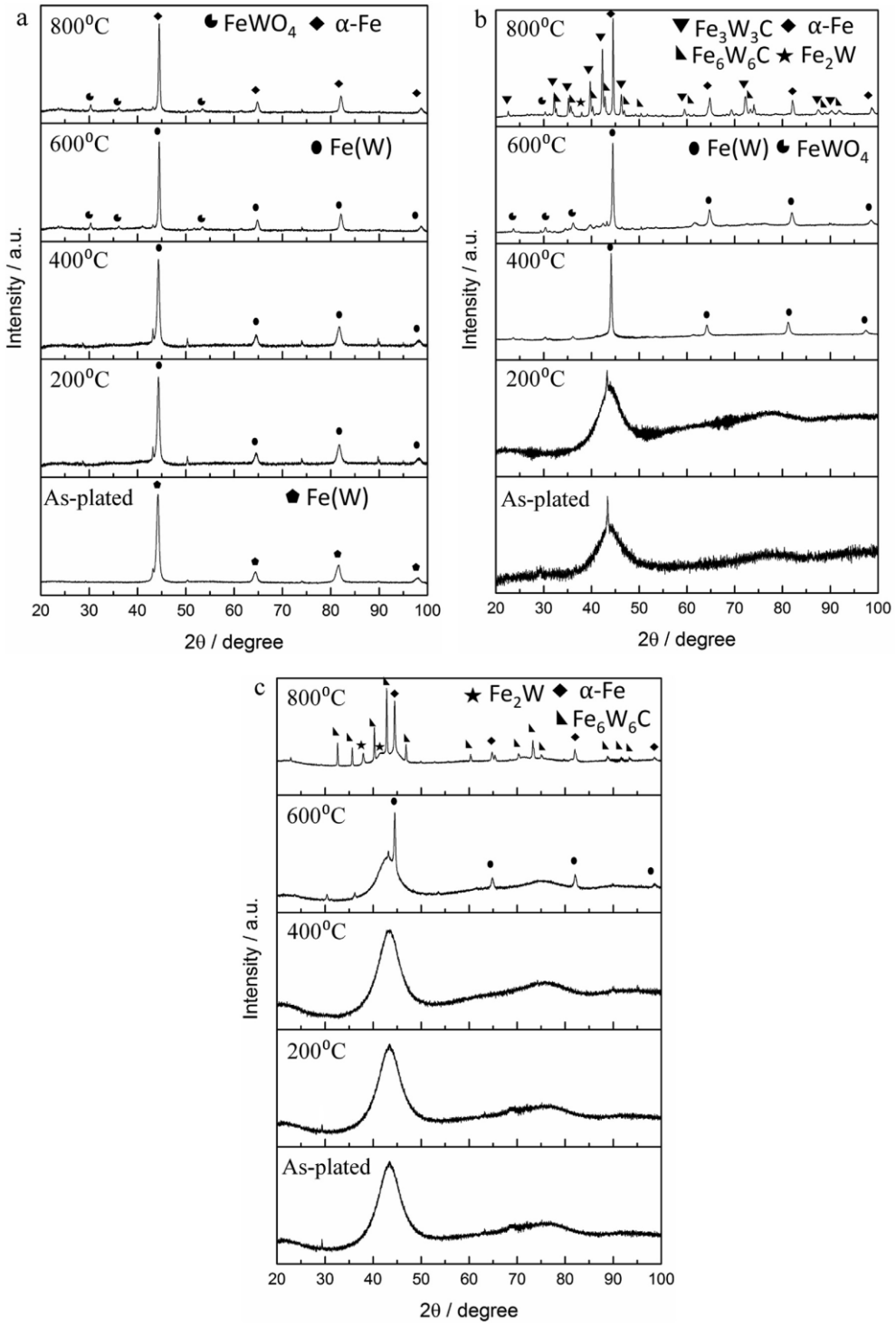

Fig. 7. X-ray diffraction patterns for Fe-W alloys with 4 at.% of W (a), 16 at.% of W (b), and 24 at.% of W (c) annealed at different temperatures.

Krasinov and A. Krasinov [44], the appearance of co-deposited O could be attributed to the interaction of intermediate particle of iron-group metal with absorbed refractory metal anion resulting in the formation of intermediate heterometallic cluster which is subsequently reduced. It can be supposed that at elevated temperatures

the rate of the second step reaction is significantly higher, thus, formed intermediates are reduced faster without the formation of oxygen-containing admixtures [45].
XRD results of the as-plated Fe-W coatings are shown in Fig. 5. The X-ray diffraction profile of the sample deposited with 4 at.% W shows the presence of crystalline peaks which are indexed as an Fe(W) solid solution. This is in accordance with previous findings: with relative low W content, a solid solution is formed and the deposited alloys retain the structure of the base metal, in this case bcc-iron (Im3m), with an increased lattice parameter due to W substitution in the bcc lattice [12]. For W concentrations ranging from 11.5 at.% to 20 at.% Nishi et al. [46] have found that the Fe-W alloy could be deposited from simple citrate bath with either a crystalline, an amorphous or a mixed amorphous-crystalline structure. In this window of W composition they found that the pH of the electrolytic bath and the current density applied for the deposition had an influence on the as-deposited Fe-W structure. For a W content higher than 20 at.%, the deposited Fe-W alloys are instead fully amorphous [13,43,47], or possess a nanocrystalline structure [14,48]. Similar findings are observed from the X-ray diffraction patterns of the samples deposited with 16 at.% and 24 at.% W: a broad peak starts around 40_ indicating the amorphous nature of both coatings. Though, a small crystalline peak appears at the top of the amorphous shoulder of the sample with 16 at.% W, indicating a certain degree of crystallinity to be present in this case. However, it is hard to distinguish solely by XRD measurements between a totally amorphous structure and a partially crystalline structure formed by the aggregation of crystals at the nanoscale. The presence of such nano-crystals would in fact as well cause a broad diffraction peak [49]. The Fe-W sample with 24 at.% W was analyzed with TEM to confirm the amorphous nature deduced from the XRD results. Fig. 6a shows the TEM bright-field image of the sample surface while Fig. 6b shows the selected area diffraction pattern (SAD). Both the TEM micrograph and the diffuse rings of the SAD pattern are typically observed in amorphous samples.

3.2. Characterization of annealed coatings

Vacuum annealing tests were performed on three selected samples, 4 at.%, 16 at.% and 24 at.% W, to study the thermal stability of the Fe-W coatings and the structural changes occurring at high temperature. The XRD profiles of the annealed samples with increasing W content are shown in Fig. 7. All the phases formed at their respective temperature, listed in Table 2, were compared with the phases expected from the binary equilibrium phase diagrams

shown in Fig. 8. Fig. 8a corresponds to the binary Fe-W phase diagram, while Fig. 8b represents a Fe-W-C phase diagram as obtained by using Thermo-Calc software [50]. The amount of carbon was fixed to 2.5 at.%, which is the quantity found at a depth of 1.5 mm in both the sample with 4 at.% and 16 at.% of W.

There are minor changes in the XRD patterns acquired before and after the heat treatment for the coating deposited with 4 at.% of W. When increasing the temperature, the indexed Fe(W) solid solution peak of the as-deposited coating is shifted toward higher diffraction angles, approaching the diffraction angle of pure a-Fe. Small amounts of W probably remain dissolved in the crystal structure of the a-Fe phase because the maximum solubility of W in the a-Fe at 800 _C is 1.2 at.%, from the data acquired from Fig. 8a. The small peaks appearing at 600 _C are indexed as an irontungsten oxide phase and are also found at 800 _C. It can be excluded that this phase is formed during the annealing due to some oxygen contamination. Hence, phase formation can be inferred to the high level of oxygen co-deposited within the coating, as shown by GD-OES measurements (Fig. 4a).

The XRD profiles acquired at different temperatures of both 16 at.% Wand 24 at.% W show that the samples are deposited in a metastable state and undergo phase transformation when exposed to elevated temperatures. Yet, the recrystallization process differs for these two samples (here and in the following the term recrystallization is used to describe the formation of crystalline phases upon annealing). The structure of the Fe-W sample having 16 at.% of W appears to be unaffected up to 200 _C. However, after heating at 400 _C recrystallization is observed. All crystalline peaks are identified and indexed as Fe(W) solid solution. Afterwards, the recrystallization proceeds similarly to what is seen in the 4 at.% W sample: the Fe(W) peak is approaching the diffraction angle of pure a-Fe and new stable phases are formed. At 600 _C small $FeWO_4$ peaks are visible, while at 800 _C two carbide phases, Fe_3W_3C and Fe_6W_6C, and the intermediate Fe_2W phase are also observed to occur. The formation of such carbides has been previously reported when performing annealing of electrodeposited Fe-W alloys [43,47] as well as for Ni-W alloys [19] because the presence of carbon in bulk is proved to be unavoidable in the electroplating process, and carbides begin to form at very low carbon concentrations. It has been shown that ~4 at.% of C is enough to form the carbide phase annealing at 800 _C. That amount of carbon can be easily codeposited within the coating when organic complexing agents or additives are used [30]. Furthermore, the obtained phases a-Fe, $Fe_2W$and Fe_3W_3C at 800 _C are shown to be stable (see Fig. 8b). As a matter of fact, the M6C phase obtained by Thermo-Calc is a carbide

with atomic ratio almost identical to the Fe3W3C phase.
The Fe-W having 24 at.% W annealed at 600 _C remains partially amorphous (the broad amorphous peak is still present), and the

Table 2
Phases forming at each respective temperature for the annealed samples.

Temperature	Phase		
	4 at.%W	16 at.%W	24 at.%W
As-deposited	$Fe_{0.96}W_{0.04}$ (PDF-04-006-3509) Cu (PDF-00-004-0836)	amorphous	amorphous
200 °C	$Fe_{0.98}W_{0.02}$ (PDF-04-004-2476)	amorphous	amorphous
400 °C	$Fe_{0.98}W_{0.02}$ (PDF-04-004-2476)	$Fe_{0.96}W_{0.06}$ (PDF-04-003-5513)	amorphous
600 °C	$Fe_{0.98}W_{0.02}$ (PDF-04-004-2476) $FeWO_4$ (PDF-01-074-1130)	$Fe_{0.98}W_{0.02}$ (PDF-04-004-2476) $FeWO_4$ (PDF-01-074-1130)	α-Fe (PDF-04-007-9753)
800 °C	α-Fe (PDF 04-007-9753) $FeWO_4$ (PDF-01-074-1130)	α-Fe (PDF 04-007-9753) $FeWO_4$ (PDF-01-074-1130) Fe_3W_3C (PDF 01-089-2579) Fe_6W_6C (PDF 04-003-9466) Fe_2W (PDF 01-075-7894)	α-Fe (PDF 04-007-9753) Fe_6W_6C (PDF 04-003-9466) Fe_2W (PDF 01-075-7894)

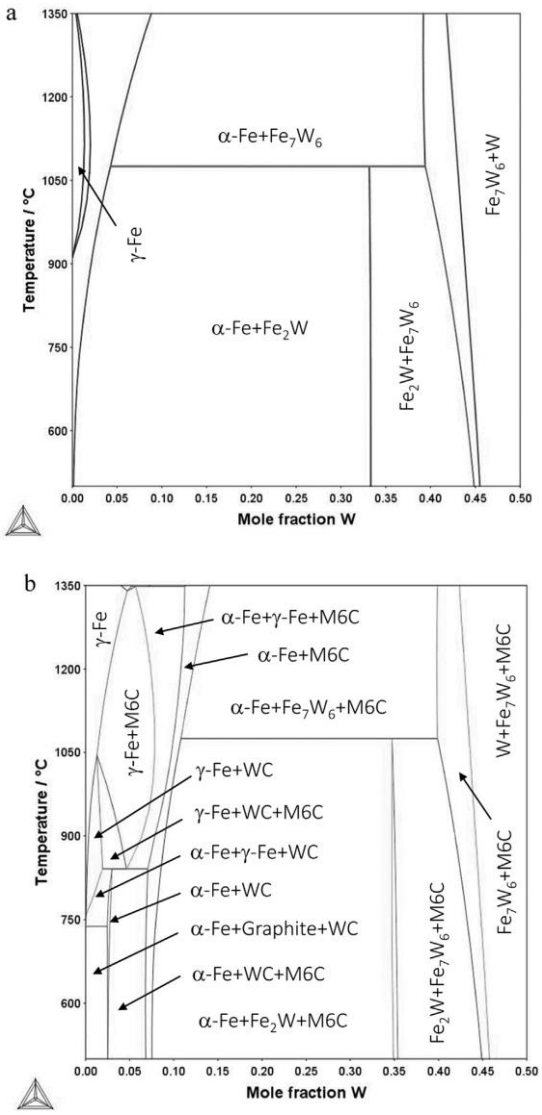

Fig. 8. Fe-W phase diagram (a) and Fe-W-C phase diagram (b) computed using Thermo-Calc software. M6C denotes a Fe-W-C phase with ~43 at.% Fe, 43 at.% W and 14 at.% C.

first crystalline phase formed is indexed as a-Fe. The amount of crystalline phase was estimated to be around 24%. This percentage was obtained by dividing the area of the crystalline peaks by the total area of the XRD spectrum. The same behavior was reported for Fe-W alloys with similar W content electrodeposited from Fe(II)-based citrate bath [43] and Fe(III)-based citrate-ammonia bath [14]. Remarkably, for Co-W alloys a well-developed polycrystalline structure appears already at 400 _C [15]. Thus, Fe-W alloys could be considered as more thermally stable coatings. At 800 _C, a-Fe formation is accompanied by two additional phase, i.e. Fe_6W_6C and Fe_2W, also found after heat treatment of the sample with 16 at.% W. However, the Fe_3W_3C phase is not observed in the Fe-24 at.% W samples. Possible explanations to this behavior can be the following: the lower amount of carbon found within the sample with 24 at.% W, and the incomplete recrystallization after annealing for 1 h at 800 _C. As a matter of fact, for the samples with 4 at.% W and 16 at.% W, the carbon content is varying between 1.5 and 2.5 at.% at a distance of 5 mm below the surface. For the sample with 24 at.% W, in the same window of thickness, the carbon is ranging from 0.2 to 0.4 at.%. In addition, the Fe_3W_3C phase requires a higher amount of carbon to be formed with respect to the Fe_6W_6C phase. The other reason is concerning the incomplete recrystallization of the sample with 24 at.% W, since the broader amorphous peak is still partially visible in the XRD diffractogram acquired at 800 _C. The Fe_3W_3C peaks may be hidden within the remaining amorphous region. The reason for this incomplete recrystallization can be referred to the higher thermal stability of this sample. The higher thermal stability can be related to the lower rate of elemental diffusion obtained when adding a higher melting point element in the alloy, like in the case of W addition [3].

Heat treatment results can also be used to distinguish between a homogenous amorphous phase from a mixed amorphous crystalline phase [49]. Thus, the different recrystallization process observed for the three annealed samples can help to define if the crystallographic state of the as-deposited sample with 16 at.% W is indeed not fully amorphous. As previously stated the structural changes upon heating of this sample are similar to those observed for the sample with 4 at.% W. With increasing annealing temperature, the small crystalline peak at the top of the broad amorphous shoulder sharpens and is indexed as a supersaturated Fe(W) solid solution which approaches the diffraction angle of pure a-Fe at 800 _C. This strengthens the hypothesis of the pre-existence of a crystalline phase in the sample in the as-plated state. The fully amorphous sample with 24 at.% W crystallizes instead by forming directly the equilibrium phases expected from the phase diagram:

first a-Fe at 600 _C, and then the Fe_6W_6C carbide phase, and the Fe_2W laves phase at 800 _C.
The structural changes occurring in the samples upon annealing are observable from the morphology changes shown in Fig. 9. Here, the surface for each sample annealed at 800 _C is shown. After annealing, the morphology of the sample with 4 at.% W changes slightly: the globular structure observed in the as-plated state is still found, but it appears more compact with small crystallites on the top. Instead, major changes are visible for both the samples with 16 at.% W and 24 at.% W due to the recrystallization of the amorphous phase. Small crystallites homogeneously distributed appear on both surfaces as seen in Fig. 9b and c, where according to GD-OES the surface of both was contaminated with relatively high amounts of carbon (Fig. 4). At the surface of the sample with 16 at.% W the carbides formation is evident: see the clusters of round shape in Fig. 9b. Local EDS point analysis revealed that these features are W-rich clusters, reaching tungsten contents up to 45 at.%. Such contents fit with the W concentration present in the carbide phases. But the carbides appear to be also distributed along the surface of the 24 at.% W sample: small W-rich clusters are clearly visible when imaging with backscattered electrons.

4. Conclusions

In-depth characterization of composition and structure of electrodeposited Fe-W alloys from developed glycolate-citrate bath has been done. Annealing experiments were performed in order to estimate the thermal stability of Fe-W coatings and to trace the structural changes occurring in alloys of different composition. Based on the results presented in this study the following conclusions can be drawn:
_ According to the obtained GD-OES CDPs, electrodeposited Fe-W alloys contain up to 80 at.% of O, 10 at.% of C and few at.% of H at the top of the coatings, and the content of these elements decreases sharply within 0.5e0.7 mm. Only for an alloy with low W content we found ~7 at.% of O distributed along the entire film thickness. This correlates with intensive side reactions that occurred at room temperature deposition and caused the internal crack formation and increased the porosity of the coating.
Carbon is present in three analyzed coatings in a lower concentration as compared to the surface: i.e. ~1e2 at.% for the samples with 4 at.% and 16 at.% W, and ~0.3 at.% for the sample with 24 at.% W.
_ The XRD patterns acquired from the as-plated samples show how the crystallographic structure of the Fe-W coatings changes

with increasing W content: a nanocrystalline structure is found for the 4 at.% W sample, a mixed nanocrystalline-amorphous structure for the sample with 16 at.% W, and a homogenous amorphous nature for the 24 at.% W sample. TEM analysis of the sample with 24 at.% W confirmed its amorphous structure.
_ The thermal stability was evaluated in the range of 200 _Ce800 _C. Annealing coupled with XRD analysis show that the thermal stability of Fe-W alloys increases with the W content. The Fe-W sample with 24 at.% W retains the amorphous structure up to 600 _C, where a partially crystalized structure was observed. Furthermore, the different recrystallization process observed for the three annealed samples helped to clarify the structural difference between the mixed nanocrystalline amorphous phase of the sample with 16 at.% W and the homogenous amorphous phase of the 24 at.% W sample.
_ The formation of carbide phases after annealing at 800 _C was noticed for alloys having 16 and 24 at.% of W. Two carbide phases, i.e. Fe_3W_3C and Fe_6W_6C, are observed after heat treatment of the 16 at.% W sample, while just the Fe_6W_6C phase is formed after heat treatment of the 24 at.% W sample. Possible explanations to this behavior are the lower amount of carbon found within the sample with 24 at.% W, and its incomplete recrystallization after annealing for 1 h at 800 _C.

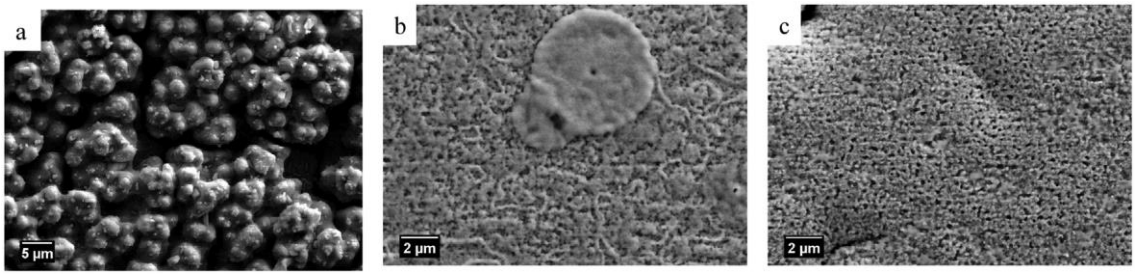

Fig. 9. SEM imaging of the surface morphology of the Fe-W alloy with 4 at.% W (a), 16 at.% W (b) and 24 at.% W (c) after annealing at 800 _C.

Acknowledgements

This work has been funded by the European Union's Horizon 2020 research and innovation programme under the Marie Skłodowska-Curie grant agreement No 642642 (SELECTA) and Moldavian National Project (15.817.02.05A).

References

[1] S.-J. Mun, M. Kim, T.-H. Yim, J.-H. Lee, T. Kang, Mechanical and structural characteristics of electrodeposited NieFeeW alloy after heat-treatment, J. Electrochem. Soc. 157 (2010) D177eD180, https://doi.org/10.1149/1.3292282.

[2] M.X. Donten, H. Cesiulis, Z. Stojek, Electrodeposition and properties of Ni-W, Fe-W and Fe-Ni-W amorphous alloys. A comparative study, Electrochim. Acta. 45 (2000) 3389e3396, https://doi.org/10.1016/S0013-4686(00)00437-0.

[3] F. He, J. Yang, T. Lei, C. Gu, Structure and properties of electrodeposited Fe-Ni-W alloys with different levels of tungsten content: a comparative study, Appl. Surf. Sci. 253 (2007) 7591e7598, https://doi.org/10.1016/j.apsusc.2007.03.068.

[4] A. Chianpairot, G. Lothongkum, C.A. Schuh, Y. Boonyongmaneerat, Corrosion of nanocrystalline Ni-W alloys in alkaline and acidic 3.5wt.% NaCl solutions, Corros. Sci. 53 (2011) 1066e1071, https://doi.org/10.1016/j.corsci.2010.12.001.

[5] P. de Lima-Neto, G.P. da Silva, A.N. Correia, A comparative study of the physicochemical and electrochemical properties of Cr and Ni-W-P amorphous electrocoatings, Electrochim. Acta. 51 (2006) 4928e4933, https://doi.org/10.1016/j.electacta.2006.01.036.

[6] N. Tsyntsaru, H. Cesiulis, A. Budreika, X. Ye, R. Juskenas, J.P. Celis, The effect of electrodeposition conditions and post-annealing on nanostructure of Co-W coatings, Surf. Coatings Technol. 206 (2012) 4262e4269, https://doi.org/10.1016/j.surfcoat.2012.04.036.

[7] A. Nicolenco, N. Tsyntsaru, H. Cesiulis, Fe (III)-based ammonia-free bath from electrodeposition of Fe-W alloys, J. Electrochem. Soc. 164 (9) (2017) D590eD596, https://doi.org/10.1149/2.1001709jes.

[8] E.P. Barbano, I. Carlos, E. Vall_es, Electrochemical synthesis of Fe-W and Fe-W-P magnetic amorphous films and Fe-W nanowires, Surf. Coat. Technol. 324 (2017) 80e84, https://doi.org/10.1016/j.surfcoat.2017.05.071.

[9] I.Y. Yermolenko, M.V. Ved, N.D. Sakhnenko, Y.I. Sachanova, Composition, morphology, and topography of galvanic coatings Fe-Co-W and Fe-Co-Mo, Nanoscale Res. Lett. 12 (1) (2017) 352, https://doi.org/10.1186/s11671-017-2128-3.

[10] G. Yar-Mukhamedova, M. Ved, N. Sakhnenko, A. Karakurkchi, I. Yermolenko, Iron binary and ternary coatings with molybdenum and tungsten, Appl. Surf. Sci. 383 (2016) 346e352, https://doi.org/10.1016/j.apsusc.2016.04.04.

[11] Y.D. Gamburg, E.N. Zakharov, G.E. Goryunov, Electrodeposition, structure, and properties of iron e tungsten alloys 37 (2001) 670e673.

[12] N. Tsyntsaru, H. Cesiulis, M. Donten, J. Sort, E. Pellicer, E.J. Podlaha-Murphy, Modern trends in tungsten alloys electrodeposition with iron group metals, Surf. Eng. Appl. Electrochem 48 (2013) 491e520, https://doi.org/10.3103/S1068375512060038.

[13] M. Donten, Bulk and surface composition, amorphous structure, and thermocrystallization
of electrodeposited alloys of tungsten with iron, nickel, and
cobalt, J. Solid State Electrochem 3 (1999) 87e96, https://doi.org/10.1007/s100080050133.

[14] N. Tsyntsaru, J. Bobanova, X. Ye, H. Cesiulis, A. Dikusar, I. Prosycevas, J.P. Celis, Iron-tungsten alloys electrodeposited under direct current from citrateammonia

plating baths, Surf. Coat. Technol. 203 (2009) 3136e3141, https://doi.org/10.1016/j.surfcoat.2009.03.041.
[15] N. Tsyntsaru, H. Cesiulis, E. Pellicer, J.P. Celis, J. Sort, Structural, magnetic, and mechanical properties of electrodeposited cobalt-tungsten alloys: intrinsic and extrinsic interdependencies, Electrochim. Acta 104 (2013) 94e103, https://doi.org/10.1016/j.electacta.2013.04.022.
[16] R. Scully, A. Gebert, J.H. Payer, Corrosion and related mechanical properties of bulk metallic glasses, J. Mater. Res. 22 (2007) 302e313, https://doi.org/10.1557/jmr.2007.0051.
[17] A. Nicolenco, N. Tsyntsaru, J. Fornell, E. Pellicer, J. Reklaitis, D. Baltrunas, H. Cesiulis, J. Sort, Mapping of magnetic and mechanical properties of Fe-W alloys electrodeposited from Fe(III)-based glycolate-citrate bath, Mater. Des. 139 (2018) 429e438, https://doi.org/10.1016/j.matdes.2017.11.011.
[18] C.J. Marvel, D. Yin, P.R. Cantwell, M.P. Harmer, The influence of oxygen contamination on the thermal stability and hardness of nanocrystalline Ni-W alloys, Mater. Sci. Eng. A 664 (2016) 49e57, https://doi.org/10.1016/j.msea.2016.03.129.
[19] C.J. Marvel, P.R. Cantwell, M.P. Harmer, The critical influence of carbon on the thermal stability of nanocrystalline Ni-W alloys, Scr. Mater. 96 (2015) 45e48, https://doi.org/10.1016/j.scriptamat.2014.10.022.
[20] S. Hayata, S. Oue, H. Nakano, T. Takahash, Effect of annealing on the structure and hardness of electrodeposited Ni-W alloys, ISIJ Int. 5 (2015) 1083e1090, https://doi.org/10.2355/isijinternational.55.1083.
[21] Z. G_alikov_a, M. Chovancov_a, V. Danielik, Properties of Ni-W alloy coatings on steel substrate, Chem. Pap. 60 (2006) 353e359, https://doi.org/10.2478/s11696-006-0064-2.
[22] S. Oue, H. Nakano, S. Kobayashi, H. Fukushima, Structure and codeposition behavior of NieW alloys electrodeposited from ammoniacal citrate solutions, J. Electrochem. Soc. 156 (2009) D17eD22, https://doi.org/10.1149/1.3006389.
[23] T. Yamasaki, P. Schlossmacher, K. Ehrlich, Y. Ogino, Formation of amorphous electrodeposited Ni-W alloys and their nanocrystallization, Nanostruct. Mater. 10 (1998) 375e388, https://doi.org/10.1016/S0965-9773(98)00078-6.
[24] Y. Kimoto, A. Giga, T. Ohkubo, Y. Takigawa, K. Hono, K. Higashi, Ni-W amorphous/nanocrystalline duplex composite produced by electrodeposition, Mater. Trans. 48 (2007) 996e1000, https://doi.org/10.2320/matertrans.48.996.
[25] R. Ju_skenas, I. Valsiunas, V. Pak_stas, R. Giraitis, On the state of W in electrodeposited
Ni-W alloys, Electrochim. Acta 54 (2009) 2616e2620, https://doi.org/10.1016/j.electacta.2008.10.060.
[26] A.J. Detor, C.A. Schuh, Microstructural evolution during the heat treatment, J. Mater. Res. 22 (2007) 3233e3248, https://doi.org/10.1557/JMR.2007.0403.
[27] A.J. Detor, M.K. Miller, C.A. Schuh, Solute distribution in nanocrystalline NieW alloys examined through atom probe tomography, Philos. Mag. 86 (2006) 4459e4475, https://doi.org/10.1080/14786430600726749.
[28] E. Dislaki, J. Sort, E. Pellicer, Parametric aqueous electrodeposition study and characterization of FeeCu films, Electrochim. Acta 231 (2017) 739e748, https://doi.org/10.1016/j.electacta.2017.02.092.
[29] J. George, S. Elhalawaty, A.J. Mardinly, R.W. Carpenter, D. Litvinov, S.R. Brankovic, Oxide/hydroxide incorporation into electrodeposited CoFe alloys - consequences for magnetic softness, Electrochim. Acta 110 (2013) 411e417, https://doi.org/10.1016/j.electacta.2013.06.097.

[30] Y.D. Gamburg, G. Zangari, Theory and Practice of Metal Electrodeposition, 2011, https://doi.org/10.1017/CBO9781107415324.004.
[31] J. Angeli, A. Bengtson, A. Bogaerts, V. Hoffmann, V.-D. Hodoroaba, E. Steers, Glow discharge optical emission spectrometry: moving towards reliable thin film analysisea short review, J. Anal. At. Spectrom. 18 (2003) 670e679, https://doi.org/10.1039/B301293J.
[32] V. Hoffmann, S. Donath, H. Merker, Verfahren zur Herstellung von massiven Kalibrationsproben für die analytische Spektrometrie, DE 102013225940 B3.
[33] V. Hoffmann, Massive wasserstoffhaltige vakuumdichte Proben, Verfahren zu ihrer Herstellung und Verwendung, DE 102013225940 B3.
[34] L. Wilken, V. Hoffmann, K. Wetzig, Erosion rate measurements for GD-OES, J. Anal. At. Spectrom. 18.9 (2003) 1141e1145.
[35] C. Gonzalez-Gago, P. Smid, T. Hofmann, C. Venzago, V. Hoffmann, W. Gruner, The use of matrix-specific calibrations for oxygen in analytical glow discharge spectrometry, Anal. Bioanal. Chem. 406 (2014) 7473e7482, https://doi.org/10.1007/s00216-014-8186-9.
[36] M. K€oster, Poster Presentation PW96 CSXXXVI, 2009.
[37] V. Hoffmann, 8th Nordic Conference on Plasma Spectrochemistry.
[38] L. Oniciu, L. Muresan, Some fundamental aspects of levelling and brightening in metal electrodeposition, J. Appl. Electrochem. 21 (1991) 565e574, https://doi.org/10.1007/BF01024843.
[39] O. Younes, E. Gileadi, Electroplating of Ni-W alloys. I. Ammoniacal citrate baths, J. Electrochem. Soc. 149 (2002) C100eC111, https://doi.org/10.1149/1.1433750.
[40] A. Kola, X. Geng, E.J. Podlaha, AgeWelectrodeposits with highWcontent from thioureaecitrate electrolytes, J. Electroanal. Chem. 761 (2016) 125e130.
[41] W. Cao, C. Marvel, D. Yin, Y. Zhang, P. Cantwell, M.P. Harmer, J. Luo, R.P. Vinci, Correlations between microstructure, fracture morphology, and fracture toughness of nanocrystalline Ni-W alloys, Scr. Mater. 113 (2016) 84e88, https://doi.org/10.1016/j.scriptamat.2015.09.030.
[42] P. Egberts, P. Brodersen, G.D. Hibbard, Mesoscale structure in electrodeposited nanocrystalline Ni-Fe alloys, Mater. Sci. Eng. A 441 (2006) 336e341, https://doi.org/10.1016/j.msea.2006.08.023.
[43] S. Wang, C. Zeng, Y. Ling, J. Wang, G. Xu, Phase transformations and electrochemical
characterizations of electrodeposited amorphous FeeWcoatings, Surf. Coat. Technol. 286 (2016) 36e41, https://doi.org/10.1016/j.surfcoat.2015.12.011.
[44] V. Krasinov, A. Krasinov, Mechanism for induced codeposition of alloys and some single refractory metals, Khimiya I Khimicheskaya Tekhnologiya 37 (2016) 8e14, https://doi.org/10.15217/issn1998984-9.2016.37.8.
[45] V. Krasinov, The role of electrochemical cobalt reduction intermediates in the formation of oxygen-containing admixtures, Khimiya I Khimicheskaya Tekhnologiya 31 (2015) 40e46, https://doi.org/10.15217/issn1998984-9.2015.31.40.
[46] Y. Nishi, Y. Mogi, K. Oguri, T. Watanabe, Preparation of F e-W amorphous films by an electroplating method, J. Mater. Sci. Lett. 20 (1995) 1e3.
[47] M.C. Chou, C.F. Chu, S.T. Wu, Phase transformations of electroplated amorphous iron-tungsten-carbon film, Mater. Chem. Phys. 78 (2003) 59e66, https://doi.org/10.1016/S0254-0584(02)00217-1.
[48] Z.I. Bobanova, A.I. Dikusar, H. Cesiulis, J.-.P. Celis, N.I. Tsyntsaru, I. Prosycevas,

Micromechanical and tribological properties of nanocrystalline coatings of irontungsten alloys electrodeposited from citrate-ammonia solutions, Russ. J. Electrochem. 45 (2009) 895e901, https://doi.org/10.1134/S1023193509080096.
[49] F. Wang, K. Itoh, T. Watanabe, Relationship between the crystallographic structure of electrodeposited FeeP alloy film and its thermal equilibrium phase diagram 44 (2003) 127e132, https://doi.org/10.2320/matertrans.44.127.
[50] J.O. Andersson, T. Helander, L. H€oglund, P.F. Shi, B. Sundman, Thermo Calc and DICTRA, computational tools for material science, Calphad 26 (2002) 273e312, https://doi.org/10.1016/S0364-5916(02)00037-8.